J. Fluid Mech. (2005), *vol.* 545, *pp.* 113–139.
doi:10.1017/S0022112005006877 Printed in the United Kingdom

On the effect of inertia and history forces on the slow motion of a spherical solid or gaseous inclusion in a solid-body rotation flow

By FABIEN CANDELIER, JEAN-RÉGIS ANGILELLA AND MOHAMED SOUHAR

Laboratoire d'Énergétique et de Mécanique Théorique et Appliquée, CNRS UMR 7563, INPL, 2 av. de la Forêt de Haye, BP 160, 54 504 Vandœuvre-Lès-Nancy, France

(Received 20 September 2004 and in revised form 16 June 2005)

The motion of a spherical inclusion released in a vertical solid-body rotation flow is investigated theoretically and experimentally. Solid spheres and bubbles are considered. The particle Reynolds number, the Taylor number, the Weber number and the capillary number are smaller than unity. The motion equations of the inclusion are obtained by revisiting the hydrodynamic equations. The axial (vertical) motion and the horizontal motion are uncoupled, even though they are sensitive to the rotation rate of the flow. Analytical solutions of the particle motion equation are compared to experimental results obtained by releasing a particle in a rotating tank filled with silicone oil. For solid spheres and bubbles, both the terminal velocity and the particle ejection rate (or trapping rate) predicted by the theory agree with experiments, without any empirical adjustment. In particular, the experimental device enables us to check the validity of various theories involving solid or gaseous inclusions with or without inertia or history effects. It is observed that the mobility tensor obtained by writing the fluid motion equations in the rotating frame accurately predicts the horizontal particle trajectory, like the Boussinesq–Basset equation obtained by writing the fluid motion equations in the non-rotating frame and neglecting the horizontal contribution of inertia effects.

1. Introduction

The determination of the force experienced by a spherical inclusion moving in a Newtonian fluid at low Reynolds number has been a challenging topic for several decades. This problem shows many fundamental aspects, but has obvious applications in many fields of physics or biology, as well as in engineering science. Indeed, many natural or industrial flows are loaded with solid or fluid inclusions, the scale of which can range from a few microns to several metres. The prediction of their trajectories requires a detailed understanding of their dynamics, i.e. of the force acting on them. In the present paper, the motion of a solid or gaseous inclusion in a vertical solid-body vortex is considered. This problem is of major importance for both elementary fluid dynamics and realistic situations. Indeed, this flow, though apparently simple, enables us to investigate very rich dynamical behaviours.

The motion equation of the particle in the laboratory reference frame is generally written as:

$$m_p \frac{\mathrm{d}^2 \boldsymbol{X}_p}{\mathrm{d}t^2} = m_p \boldsymbol{g} + \boldsymbol{F}^0 + \boldsymbol{F}', \tag{1.1}$$

where m_p and $\boldsymbol{X}_p(t)$ denote the particle mass and position respectively, $\boldsymbol{F}^0$ is the integral of the stress of the unperturbed velocity field $\boldsymbol{V}_f^0$ at the particle surface, and $\boldsymbol{F}'$ is the integral of the stress of the perturbation velocity field. Because the unperturbed velocity field satisfies the Navier–Stokes equations, the force $\boldsymbol{F}^0$ can be readily obtained and is often called the 'pressure gradient force of the unperturbed flow'. In particular, it includes the Archimedes force.

In contrast, it is generally difficult to find an analytical expression for $\boldsymbol{F}'$ in terms of $\boldsymbol{V}_f^0$. Nevertheless, when convective inertia effects (denoted 'inertia effects' hereinafter) can be neglected, and for an isolated solid sphere immersed in a uniform flow, $\boldsymbol{F}'$ is provided by the well-known Basset–Boussinesq–Oseen (BBO) equation (Boussinesq 1885; Basset 1888). The various terms appearing in this equation are the drag, the added-mass force and the history force. An equivalent equation for fluid inclusions immersed in an unsteady uniform flow (in the absence of inertia effects) has been obtained by Gorodtsov (1975) (see also Yang & Leal 1991; Galindo & Gerbeth 1993). The resulting force has the same form as that of Boussinesq (1885) and Basset (1888) except that the drag coefficient and the kernel in the history integral differ, since the boundary condition at the interface of the inclusion is different. Note that, for fluid inclusions, the expression of the kernel is known only in Fourier space, and no general compact expression of the force in the time-domain is available except when the viscosity ratio is either very small or very large.

Clearly, both the BBO equation and the Gorodtsov equation efficiently predict the dynamics of solid or fluid inclusions, provided inertia effects can be neglected. However, this 'creeping-flow' assumption is no longer valid in many cases. For example, when an inclusion is released into a quiescent fluid, the unsteadiness of the velocity perturbation eventually vanishes while convective terms are no longer negligible far from the inclusion (Oseen's problem). The determination of the particle-induced flow therefore requires us to solve a steady equation, but involving inertia terms; the resulting force experienced by the particle is therefore different from that of BBO or Gorodtsov. In particular, the history term vanishes and the drag coefficient increases (see Proudman & Pearson (1957) for solid particles). Note that Sano (1981), Mei & Adrian (1992) and Lovalenti & Brady (1993) have also investigated this problem for a particle moving unsteadily in a uniform flow.

If, in addition, the unperturbed flow is a shear flow, a lift force can appear owing to these inertia effects (Saffman 1965, 1968; McLaughlin 1991), as well as a shear-induced drag correction (see Harper & Chang 1968; Miyazaki, Bedeaux & Bonet Avalos 1995). Also, for particles immersed in a solid-body rotation flow, inertia effects can emerge and induce lift effects as well as drag corrections in both the axial and the radial directions (Childress 1964; Herron, Davis & Bretherton 1975; Gotoh 1990). These inertial effects have been revisited by Magnaudet (2003), and generalized to fluid inclusions, in the case of inclusions moving in a time-dependent linear flow in the vicinity of a wall (see also Legendre & Magnaudet 1997).

Several numerical investigations have been done in the last decade (see for example Magnaudet, Rivero & Fabre (1995) for history effects, and Legendre & Magnaudet (1998) for inertia effects). In contrast, very few experimental verifications of these various approaches, especially when inertial effects are present, have been done so far (see for example Odar & Hamilton (1964), Abdad & Souhar (2004*a*, *b*), Coimbra *et al.* (2004) for history effects, and Maxworthy (1965), Karanfilian & Kotas (1981) for the drag corrections due to inertia effects).

The purpose of the present paper is to investigate experimentally the history force and inertia effects experienced by a spherical solid or gaseous inclusion falling or rising in a vertical solid-body rotation flow. In addition, the radial motion of these inclusions will be investigated in detail. The question of the validity of the creeping flow assumption (i.e. no inertial effects) is of major importance in this flow. Indeed, the particle is expected to reach its terminal velocity after a short transient, so that inertial effects should be taken into account at the expense of history effects to predict the vertical motion. Nevertheless, as the particle rises (or falls) it converges towards the axis of the vortex (or is ejected towards its periphery). Under the combined effect of this radial motion and of the cylinder rotation, the fluid velocity as seen by the inclusion, in the laboratory reference frame, is unsteady. Therefore, the flow induced by the inclusion is likely to be unsteady too: history effects could therefore be non-negligible. Also, in the rotating frame, the effect of the Coriolis force on the perturbed velocity is known to induce drag corrections (see Herron *et al.* 1975).

In order to analyse these effects, we have investigated the problem in two steps. First, we have revisited the flow equations around the inclusion in order to derive the particle motion equation for both solid and gaseous inclusions. For gaseous inclusions we used the approach proposed by Legendre & Magnaudet (1997), as will be shown below. Then, we have solved analytically the particle motion equations obtained by these various theories, and relevant parameters, such as the particle ejection or trapping rate and the terminal velocity, could be obtained. Secondly, an experimental device has been built, in order to check the theoretical predictions.

Note that by writing the perturbed fluid equations in both the laboratory and the rotating frame, we are led to apparently different expressions for the hydrodynamic force experienced by the particle. This problem, investigated in detail by Miyazaki (1995), will be discussed in the conclusion of the present paper.

The effect of the Boussinesq–Basset force on the radial migration of a solid Stokes particle falling in a vertical vortex has already been investigated in detail by Candelier, Angilella & Souhar (2004), for Stokes numbers lying between 0 and 0.01. The aim of the present paper is to generalize these results to the case of gaseous inclusions and larger Stokes numbers, and to analyse the effect of rotation on the terminal vertical velocity also.

Section 2 concerns the experimental apparatus. Section 3 deals with the flow equations and the derivation of the force experienced by the inclusion. The particle motion equation is then integrated and compared to experimental results in §§ 4 and 5. A discussion is proposed in § 6.

2. Experimental apparatus

2.1. *General description*

The main facility of our experimental device is a cylindrical vertical tank made of Plexiglas. Its radius is $R = 4$ cm and its height is $L = 25$ cm. The tank rotates around its symmetry axis (figure 1). The rotation frequency can be varied from 0 to 25 rad s^{-1}, it is kept constant during the runs, and is measured with a negligible uncertainty (about 0.1 %).

The cylindrical tank is filled with silicone oil and immersed in a fixed rectangular tank also filled with the same oil (in order to account for the optical deformation through the fluids and the walls). Note that the cylindrical tank is totally hermetic so that there is no interaction between the oil located within the cylinder and the oil located in the rectangular tank. Hence, the velocity field of the oil inside the

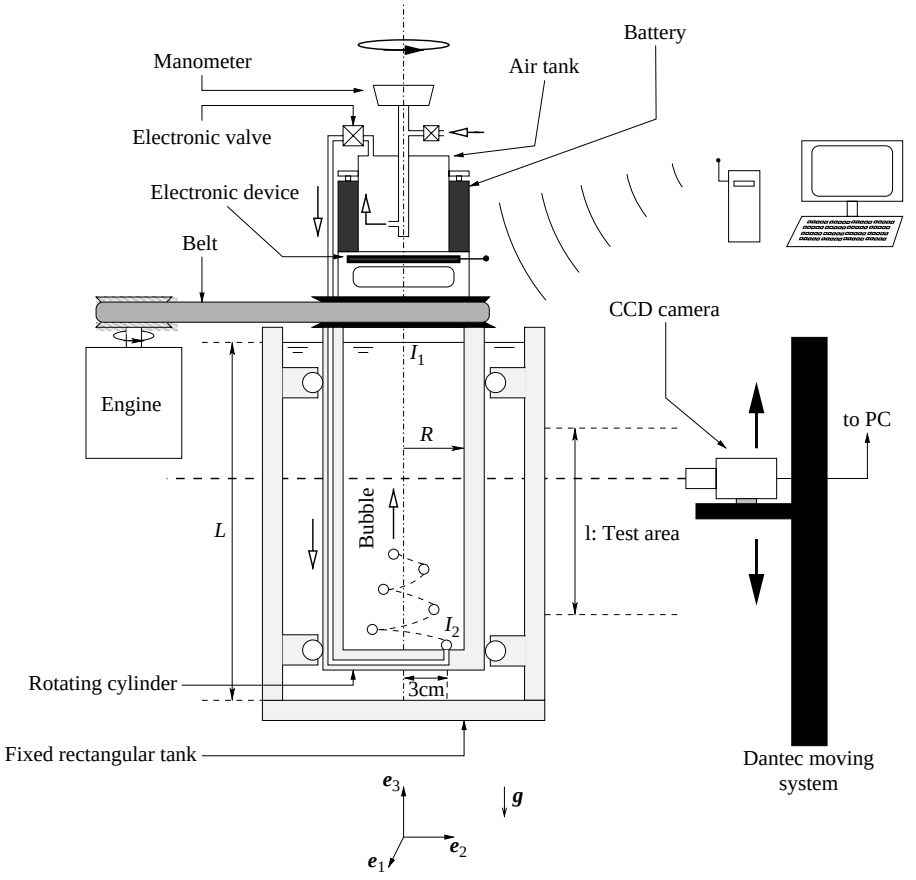

FIGURE 1. Sketch of the experimental apparatus. Solid particles are released from I_1 and bubbles are injected at I_2.

cylinder has a solid-body rotation structure a few seconds after the cylinder starts rotating. The structure of the unperturbed flow has been checked by using tracers. No differential rotation has been observed.

The kinematic viscosity of the silicone oil used for this experiment has been determined accurately by making use of a capillary viscosimeter for temperatures lying between 18 and 30 °C, and follows, with a negligible uncertainty, the linear law $\nu_f = (2.743 - 0.036\,T(^\circ\mathrm{C}))\,10^{-4}\,\mathrm{m^2\,s^{-1}}$. Its density has also been measured with an accurate densitymeter and we have $\rho_f = 972\,\mathrm{kg\,m^{-3}}$ at 20 °C. This value remains almost constant for the range of temperatures considered here.

Particles heavier than the fluid are released into the cylindrical tank through the upper lid. Bubbles are injected by means of an elaborate device described below. Because silicone oil is transparent, the inclusions are always visible. As they fall or rise, their motion is filmed by means of a CCD camera JAI CV-M30 recording 60 or 120 images $\mathrm{s^{-1}}$, according to our needs. The camera can either follow the particles along their vertical motion (by means of Dantec's moving system), or remain fixed in the laboratory reference frame. The height of the test area recorded by the camera is $l = 15\,\mathrm{cm}$ (figure 1). The resolution of the camera is about 0.3 mm $\mathrm{pixel^{-1}}$. By making use of the Optimas image processing software we can measure both the vertical and the radial coordinates of the inclusion, as well as its diameter.

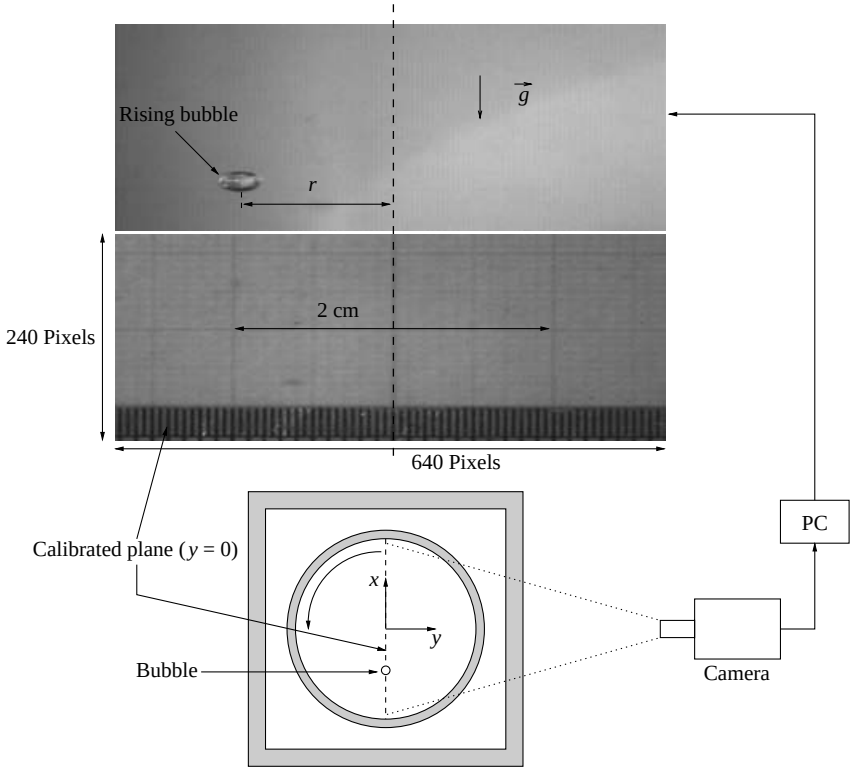

FIGURE 2. Upper view of the rotating cylinder and of the calibrated plane.

2.2. *Physical properties of the inclusions*

Two kinds of inclusion are used in the experiment: solid particles and bubbles. In the following, the index f denotes the continuous phase, whereas the index p denotes the particle, either solid or fluid. The solid particles are white polyacetal spheres, the radius of which is provided with a negligible uncertainty: $a \simeq 1.5\,\mathrm{mm}$. Their density is $\rho_p = 1410\ \mathrm{kg\,m^{-3}}$, so that the density ratio $\gamma = \rho_p/\rho_f$ is equal to 1.45 for solid spheres throughout this paper.

The gaseous inclusions used in these experiments are air bubbles, which are such that

$$\frac{\nu_p}{\nu_f} \ll 1, \quad \frac{\mu_p}{\mu_f} \ll 1, \quad \frac{\rho_p}{\rho_f} \ll 1,$$

and these properties will be used for the theoretical calculations below. Both the bubble radius and position are measured simultaneously during the motion. This can be achieved accurately by using a mobile camera moving in the vertical direction at the terminal speed of the inclusion. For example, the photograph in figure 2 shows such a bubble, together with the calibrated plane which enables us to determine both the bubble radius and position. (Note that the drop is spherical, and that the 1:2 elliptical shape is an effect due to the camera.) The absolute error about the bubble radius is one pixel, that is 0.06 mm, so that the relative error is about 4 %. As for the radial position, the absolute error is about 1 pixel, so that the relative error for the bubble in figure 2 is 0.6 %.

2.3. *The bubble injector*

Bubbles have to be injected at the bottom of the rotating cylinder, and this increases significantly the complexity of the experimental device. Gaseous inclusions are generated by a bubble injector which is fixed on the top of the rotating tank and produces bubbles at the bottom of the tank. This additional device is shown in figure 1. It is composed of a small cylindrical tank filled with air under pressure. This pressure is measured by a manometer placed above, and can be set between 0.01 and 1.5 bar. Also, an electronic valve enables us to open the air tank during a time interval τ which can be controlled accurately by using an electronic device ($5\,\mathrm{ms} \leqslant \tau < \infty$). This electronic valve is supplied by batteries which were cautiously distributed in an axisymmetric manner around the air tank, and triggered by a remote control apparatus. A tiny plastic tube joins the outlet of the electronic valve and the point I_2 at the bottom of the rotating oil tank (see figure 1). Bubbles are therefore created at point I_2, the radial position of which is $r = 3\,\mathrm{cm}$.

By controlling both the pressure in the air tank and the opening procedure of the electronic valve, we can generate isolated bubbles with a small radius distribution, so that the experiment has a satisfactory reproducibility.

2.4. *Measurement of the particle coordinates*

In the rotating case, the uncertainty about the position of the inclusion must be taken into account.

The experimental device enables us to measure the radial and vertical coordinates (r, z) of the inclusion. This can be done accurately when the particle crosses the plane $y = 0$ (see figure 2), since this position corresponds to a local maximum of the x-coordinate on the frame of the camera. The absolute error Δr due to the particle not being exactly in this plane at the time of the snapshot can be readily calculated, and satisfies $\Delta r = (r/8)(\Omega/f)^2$, where f is the camera sampling frequency, which is chosen according to the angular velocity of the rotating tank. The typical value of Δr is about 0.04 mm, so that the corresponding relative error is about 0.4 %. Therefore, the sum of the relative errors due to the pixelization (0.6 % as shown above) and to the crossing of the calibrated plane is about 1 %.

Finally, for all kinds of inclusion the angular velocity of the particle $\dot{\theta}$ is measured as follows. The time t_e elapsed between every two intersection points between the particle trajectory and the plane $y = 0$ (see figure 2) is measured accurately. In all runs, we observed that t_e is constant and very close to $2\pi/\Omega$. Therefore we concluded that the angular velocity of the particle is constant, and very close to Ω. This result will be confirmed by theoretical calculations below. Furthermore, by marking particles with spots of ink, we could observe that the proper angular velocity of the particle, Ω_p, is very close to Ω. As will be shown below, this point is in agreement with Childress' theory (Childress 1964).

2.5. *Typical trajectories and estimation of the non-dimensional parameters*

Figure 3 shows typical trajectories of solid and gaseous inclusions obtained by superimposing the images of the movies. Some orders of magnitude of the relevant non-dimensional numbers can be estimated from these photographs.

First of all, since the azimuthal slip velocity is negligible, a look at the vertical distance between every two maxima of the trajectory of figure 3 clearly shows that:

$$\frac{\mathrm{d}\boldsymbol{X}_p}{\mathrm{d}t} \cdot \boldsymbol{e}_3 = \text{constant} = V_T,$$

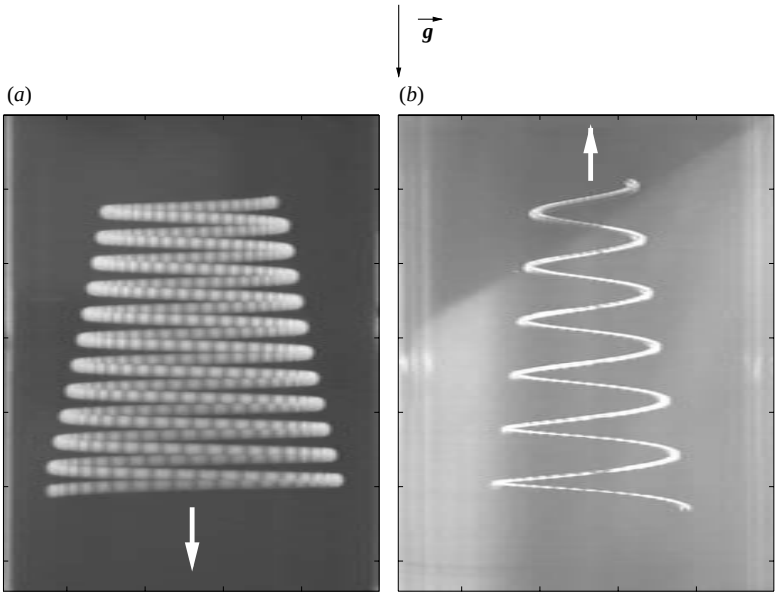

FIGURE 3. Typical trajectories in the (x,z)-plane obtained by superimposing a large number of images recorded during a run. (a) Solid sphere of radius $a = 1.5\,\text{mm}$, $\Omega = 10\,\text{rad}\,\text{s}^{-1}$, $Re_T \simeq 0.065$, $Re_H \simeq 0.004$, $S \simeq 0.012$. (b) Bubble of radius $a \simeq 1.1\,\text{mm}$, $\Omega = 7\,\text{rad}\,\text{s}^{-1}$, $Re_T \simeq 0.1$, $Re_H \simeq 0.004$, $S \simeq 0.005$. (Note that the horizontal Reynolds numbers Re_H are unsteady. The values given here correspond to the greatest speed of the inclusion during the radial migration.)

i.e. the inclusions have reached a terminal vertical velocity. This velocity is denoted by V_T in the following. We have observed that this terminal velocity is reached within a few seconds.

This observation is confirmed in figure 4 where the experimental axial coordinate of a solid sphere is plotted versus time. Clearly, the vertical velocity V_T is constant, and this constant depends on the angular velocity of the tank, as observed by Maxworthy (1965) in the absence of radial migration. (Indeed, in the experiments of Maxworthy, particles are lighter than the fluid and are injected near the axis of the tank: thus, they rise along the axis of the cylindrical tank, and experience no horizontal migration.) Maxworthy's experimental results outline the dependence of the terminal velocity on the cylinder rotation rate Ω, and are in quantitative agreement with Childress' theoretical predictions (Childress 1964). In the following the effect of Ω on the terminal velocity and the radial migration of the inclusion will be analysed for both solid and gaseous inclusions.

The vertical speed of bubbles is also constant, as shown on figure 5. It is also sensitive to Ω, as will be shown below. (Because the bubble radius slightly changes for each run, figure 5 does not show $z(t)$ for various Ω, since the bubble radius cannot be held fixed during the series of runs.)

The radial coordinate $r(t)$ of the bubble of figure 5, and the radial coordinate $r(t)$ of the solid sphere corresponding to the run $\Omega = 23\,\text{rad}\,\text{s}^{-1}$ of figure 4 are shown, respectively, in figures 6(b) and 6(a). The bubble (resp. solid particle) rises (resp. falls) with a constant speed even though it experiences a radial migration. This experimental observation suggests that the radial and the vertical motion are uncoupled. Therefore, Childress' theory is expected to be valid here, in spite of the radial motion. Moreover, these experiments show that $r(t)$ grows (resp. decays) exponentially, as observed in

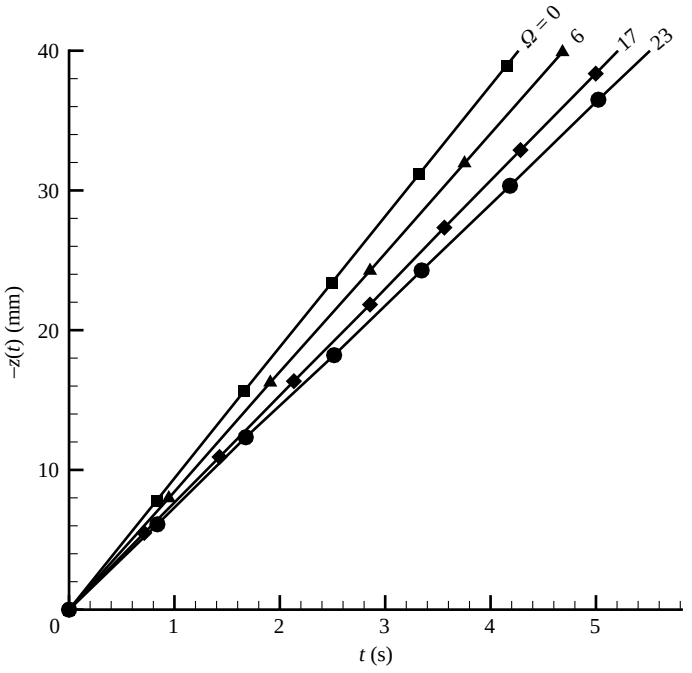

FIGURE 4. Plot of the measured vertical coordinate of a solid sphere of radius $a = 1.5\,\mathrm{mm}$ *vs.* t, for various angular velocities of the rotating cylinder (in units of $\mathrm{rad\,s^{-1}}$). For the sake of simplicity, the time $t = 0$ on figures 4 to 7 corresponds to the time when the particle reaches the test area.

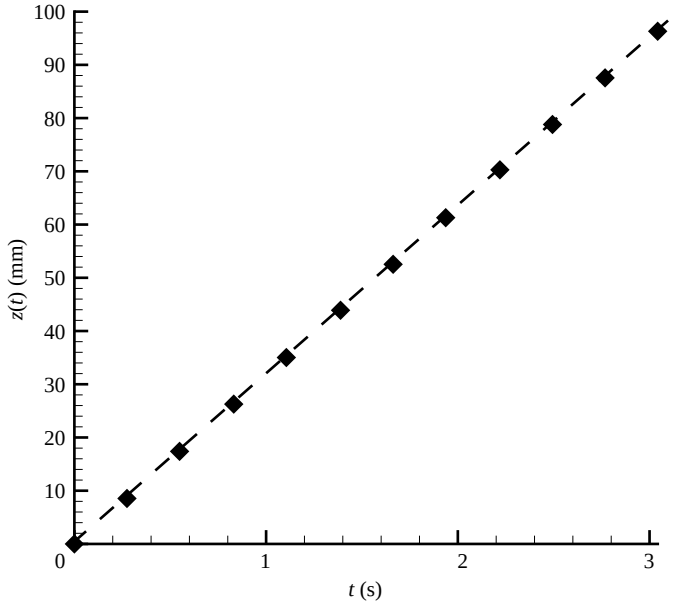

FIGURE 5. Vertical coordinate $z(t)$ of a bubble of radius $a = 1.4\,\mathrm{mm}$. The angular velocity of the tank is $\Omega = 23\,\mathrm{rad\,s^{-1}}$.

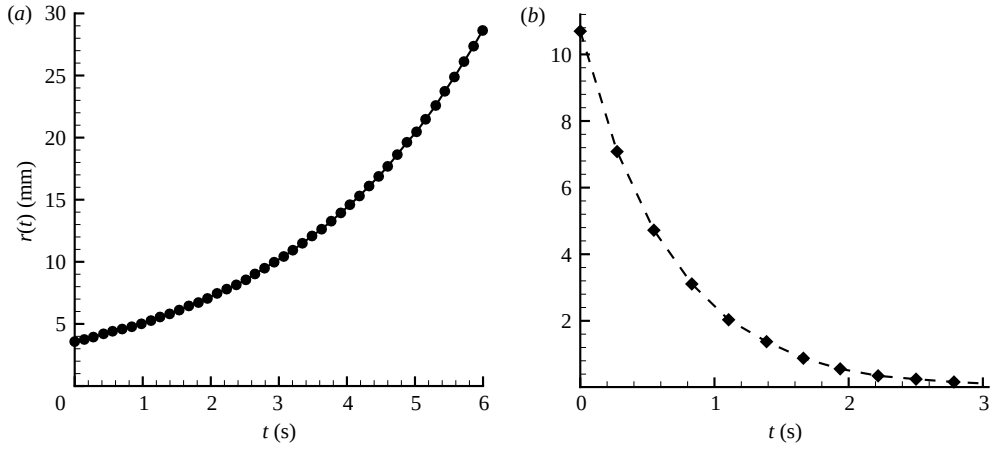

FIGURE 6. (*a*) Experimental coordinate $r(t)$ of the solid particle of figure 4 (corresponding to the run $\Omega = 23\,\mathrm{rad\,s^{-1}}$). (*b*) Experimental radial coordinate $r(t)$ corresponding to the bubble of figure 5.

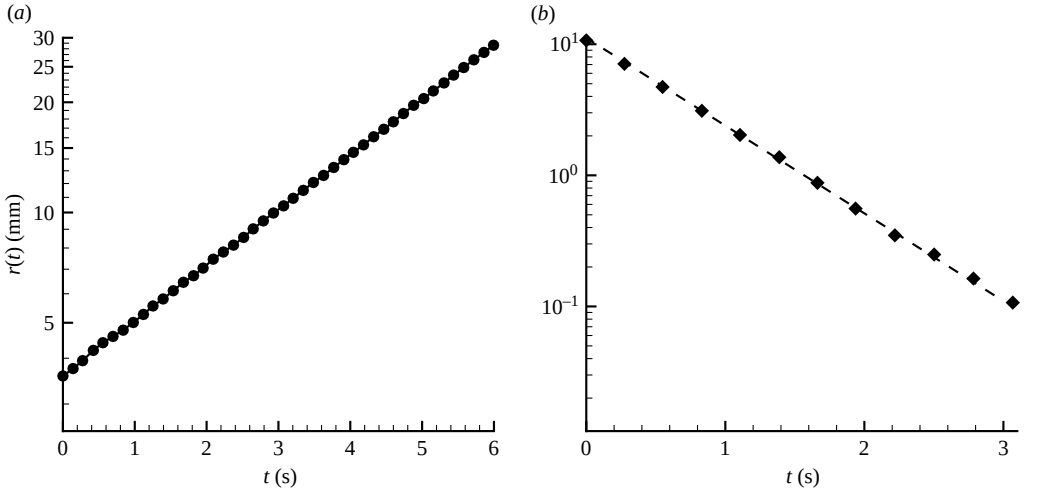

FIGURE 7. Log–linear plots of figures 6(*a*) and 6(*b*), illustrating the exponential radial migration of (*a*) solid particles and (*b*) bubbles. The dashed line and the solid line are least-squares linear fitting, the slope of which gives the experimental migration rate.

figures 7(*a*) and 7(*b*). The leading order of this exponential migration can be readily estimated, for solid particles, by solving equation (1.1) with $\boldsymbol{F}' = -6\pi\mu_f a(\boldsymbol{V}_p - \boldsymbol{V}_f^0)$ (Stokes drag). We are led to

$$r(t) \propto \exp(\lambda^0\,\Omega\,t) \quad \text{where} \quad \lambda^0 = \frac{2a^2\Omega(\gamma-1)}{9\nu_f} = 2S(\gamma-1),$$

S will be introduced below. The typical time scale $1/(\lambda^0\,\Omega)$ of this exponential will be used below to simplify the fluid motion equations. (Note that this result can be readily generalized to bubbles.)

Figure 3 also give valuable informations about the relevant non-dimensional numbers of the particle dynamics. Indeed, if δr (resp. δz) is the radial (resp. vertical)

	a (mm)	$S = \dfrac{a^2\,\Omega}{9\,\nu_f}$	$Re_T = \dfrac{aV_T}{\nu_f}$	$Re_H = \dfrac{aV_H}{\nu_f}$	$\alpha = \dfrac{18\,S}{Re_T^2}$
s	1.5	$0.006 < S < 0.029$	$0.066 < Re_T < 0.082$	$0 < Re_H < 0.09$	$20 < \alpha < 113$
g	$1.1 < a < 1.82$	$0.005 < S < 0.043$	$0.23 < Re_T < 0.41$	$0 < Re_H < 0.34$	$6 < \alpha < 40$

TABLE 1. Numerical values of the particle radius and of the non-dimensional numbers considered in this paper. (s, solid; g, gaseous) The smallest non-zero value of the angular velocity of the tank is $\Omega = 5\,\mathrm{rad\,s^{-1}}$ and its largest value is $\Omega = 23\,\mathrm{rads^{-1}}$.

distance between every two local maxima of the trajectory, these photographs suggest that:

$$\delta z = O(a), \quad \delta r = O(a),$$

where a is the radius of the inclusion. If V_H is a typical horizontal (radial) slip velocity, then $\delta r = V_H(2\pi/\Omega)$ and $\delta z = V_T(2\pi/\Omega)$, and we conclude that $V_T/a\Omega \sim V_H/a\Omega \simeq 1/2\pi = O(1)$. By multiplying these numbers by $a^2\Omega/\nu_f$ (which is much smaller than unity here), we conclude that $aV_T/\nu_f \ll 1$ and $aV_H/\nu_f \ll 1$. Let us define the following non-dimensional numbers:

$$Re_T = \frac{aV_T}{\nu_f}, \quad Re_H = \frac{aV_H}{\nu_f}, \quad S = \frac{\Omega a^2}{9\nu_f} = \frac{Ta}{9}. \tag{2.1}$$

S is the pseudo-Stokes number, and Ta is the Taylor number used by several authors (Childress 1964; Maxworthy 1965; Gotoh 1990). Accordingly, we will write

$$Re_T \ll 1, \quad Re_H \ll 1, \quad S \ll 1. \tag{2.2}$$

In particular, $\lambda^0 = O(S) \ll 1$. These assumptions will be used in the following to simplify the fluid motion equations. Note that the conclusions which have been drawn in this section are actually valid for all the runs performed in the present work.

In addition, the orders-of-magnitude of the Weber number ($\rho_f V^2 a/\sigma$) and of the capillary number ($\mu_f V/\sigma$) are less than 0.001 and 0.1, respectively ($\sigma \approx 20 \times 10^{-3}\,\mathrm{N\,m^{-1}}$ is the surface tension coefficient and V is an order-of-magnitude of either V_H or V_T).

The relevant non-dimensional numbers considered in this paper are summarized in table 1.

3. Derivation of the motion equation of the inclusion

As noted in § 1, the prediction of the vertical motion of the inclusion requires us to take convective inertia effects into account, whereas the horizontal motion is unsteady and could be sensitive to history effects. In order to clarify this point, the fluid motion equations around the inclusion are revisited in the following sections, and the results of Childress (1964) are generalized to the case of particles undergoing radial migration. The motion equation of bubbles is then derived by using the approach of Legendre & Magnaudet (1997).

3.1. *Motion equation of solid particles*

As suggested by the typical trajectories discussed above, we assume that the inclusion has reached a terminal vertical velocity $V_T \boldsymbol{e}_3$. As seen in § 1, the capital letters $\boldsymbol{X}_p$, $\boldsymbol{V}_p$ and $\boldsymbol{V}_f^0$ denote the particle position, the velocity and the fluid undisturbed velocity,

respectively, in the laboratory reference frame. It is convenient to write the fluid motion equations in the reference frame rotating with the tank:

$$\nabla \cdot \boldsymbol{v}_f = 0, \tag{3.1}$$

$$\rho_f \left(\frac{\partial \boldsymbol{v}_f}{\partial t} + (\boldsymbol{v}_f \cdot \nabla)\boldsymbol{v}_f + 2\Omega \boldsymbol{e}_3 \times \boldsymbol{v}_f \right) = -\nabla \widehat{P} + \mu_f \nabla^2 \boldsymbol{v}_f, \tag{3.2}$$

where $\boldsymbol{x} = (x, y, z)$ is the position vector and $\boldsymbol{v}_f$ is the fluid velocity in the rotating frame, and $\widehat{P}$ is the modified pressure, that is,

$$\widehat{P} = P - \tfrac{1}{2}\rho_f \Omega^2 (x^2 + y^2) + \rho_f g z.$$

The corresponding boundary conditions are

$$\boldsymbol{v}_f \to 0, \quad |\boldsymbol{x} - \boldsymbol{x}_p| \to \infty, \tag{3.3}$$

$$\boldsymbol{v}_f = \boldsymbol{v}_p(t) + \boldsymbol{\omega}_p(t) \times (\boldsymbol{x} - \boldsymbol{x}_p), \quad |\boldsymbol{x} - \boldsymbol{x}_p| = a, \tag{3.4}$$

where $\boldsymbol{x}_p$, $\boldsymbol{v}_p$ and $\boldsymbol{\omega}_p$ denote the particle position, velocity and angular velocity, respectively, in the rotating reference frame. Following Maxey & Riley (1983) we use the change of variables:

$$\boldsymbol{z} = \boldsymbol{x} - \boldsymbol{x}_p, \quad \boldsymbol{w}_f(\boldsymbol{z}, t) = \boldsymbol{v}_f(\boldsymbol{x}, t) - \boldsymbol{v}_p(t), \quad t = t$$

so that the motion equations read

$$\nabla \cdot \boldsymbol{w}_f = 0, \tag{3.5}$$

$$\rho_f \left(\frac{\partial \boldsymbol{w}_f}{\partial t} + (\boldsymbol{w}_f \cdot \nabla)\boldsymbol{w}_f + 2\Omega \boldsymbol{e}_3 \times \boldsymbol{w}_f + 2\Omega \boldsymbol{e}_3 \times \boldsymbol{v}_p \right) = -\nabla \widehat{P} + \mu_f \nabla^2 \boldsymbol{w}_f - \rho_f \frac{\mathrm{d}\boldsymbol{v}_p}{\mathrm{d}t}, \tag{3.6}$$

where

$$\boldsymbol{w}_f \to -\boldsymbol{v}_p(t), \quad |\boldsymbol{z}| \to \infty, \tag{3.7}$$

$$\boldsymbol{w}_f = \boldsymbol{\omega}_p \times \boldsymbol{z}, \quad |\boldsymbol{z}| = a. \tag{3.8}$$

We can see that in the case of a particle rising steadily along the axis of the tank, we have $\boldsymbol{v}_p(t) = V_T \boldsymbol{e}_3$, and (3.5)–(3.8), reduce to the steady problem investigated by Childress (1964). In contrast, in the present paper we have $\boldsymbol{v}_p(t) = \boldsymbol{P}_H \boldsymbol{v}_p(t) + V_T \boldsymbol{e}_3$, where $\boldsymbol{P}_H$ denotes the horizontal projection operator, so that the horizontal motion of the particle affects the surrounding velocity field through the boundary condition (3.7). In order to take advantage of Childress' solution, we introduce the new ansatz:

$$\boldsymbol{w}_f = \boldsymbol{w}^c + \boldsymbol{w}^0 + \boldsymbol{w}^1, \tag{3.9}$$

$$\widehat{P} = \widehat{P}^c + \widehat{P}^0 + \widehat{P}^1, \tag{3.10}$$

where $\boldsymbol{w}^0$ and $\widehat{P}^0$ are the unperturbed horizontal velocity and pressure fields, respectively, which are given by

$$\boldsymbol{w}^0 = -\boldsymbol{P}_H \boldsymbol{v}_p(t), \tag{3.11}$$

$$\nabla \widehat{P}^0 = 0, \tag{3.12}$$

and $\boldsymbol{w}^c$, $\widehat{P}^c$ are assumed to satisfy the following steady problem, considered by Childress (1964),

$$\nabla \cdot \boldsymbol{w}^c = 0, \tag{3.13}$$

$$\rho_f((\boldsymbol{w}^c \cdot \nabla)\boldsymbol{w}^c + 2\Omega \boldsymbol{e}_3 \times \boldsymbol{w}^c) = -\nabla \widehat{P}^c + \mu_f \nabla^2 \boldsymbol{w}^c, \tag{3.14}$$

$$\boldsymbol{w}^c \to -V_T \boldsymbol{e}_3, \quad |\boldsymbol{z}| \to \infty, \tag{3.15}$$

$$\boldsymbol{w}^c = \boldsymbol{\omega}_p \times \boldsymbol{z}, \quad |\boldsymbol{z}| = a. \tag{3.16}$$

This problem corresponds to the motion of a solid sphere moving steadily along the vertical axis of a rotating tank. By generalizing the matched asymptotic expansion approach of Kaplun & Lagerstrom (1957) and Proudman & Pearson (1957), and by taking into account inertia effects to leading order, Childress (1964) could derive an analytical expression for the drag, which will be used below.

Injecting the ansatz (3.9) into the motion equations, we are led to the following equations for the velocity field $\boldsymbol{w}^1$:

$$\nabla \cdot \boldsymbol{w}^1 = 0, \tag{3.17}$$

$$\rho_f \left(\frac{\partial \boldsymbol{w}^1}{\partial t} + (\boldsymbol{w}^1 + \boldsymbol{w}^c - \boldsymbol{P}_H \boldsymbol{v}_p) \cdot \nabla \boldsymbol{w}^1 + (\boldsymbol{w}^1 - \boldsymbol{P}_H \boldsymbol{v}_p) \cdot \nabla \boldsymbol{w}^c + 2\Omega \boldsymbol{e}_3 \times \boldsymbol{w}^1 \right) = -\nabla \widehat{P}^1 + \mu_f \nabla^2 \boldsymbol{w}^1, \tag{3.18}$$

$$\boldsymbol{w}^1 \to 0, \quad |\boldsymbol{z}| \to \infty, \tag{3.19}$$

$$\boldsymbol{w}^1 = \boldsymbol{P}_H \boldsymbol{v}_p(t), \quad |\boldsymbol{z}| = a. \tag{3.20}$$

Note that in (3.18) we made use of the fact that $(\mathrm{d}/\mathrm{d}t)\boldsymbol{P}_H \boldsymbol{v}_p = (\mathrm{d}/\mathrm{d}t)\boldsymbol{v}_p$ and $\boldsymbol{e}_3 \times \boldsymbol{P}_H \boldsymbol{v}_p = \boldsymbol{e}_3 \times \boldsymbol{v}_p$.

In order to obtain a simplified motion equation, we now focus on the various terms of (3.18). In the vicinity of the particle, the typical length scale of the perturbed velocity is the particle radius a. Moreover, the no-slip boundary conditions enable us to write

$$|\boldsymbol{w}^1| = O(v_p), \quad |\boldsymbol{w}^c| = O(V_T).$$

Therefore, the comparison between the inertia terms and the viscous terms of (3.18) leads to

$$\left| \frac{\rho_f \boldsymbol{w}^1 \cdot \nabla \boldsymbol{w}^1}{\mu_f \nabla^2 \boldsymbol{w}^1} \right| = O(a v_p / \nu_f) = O(Re_H),$$

$$\left| \frac{\rho_f \boldsymbol{w}^c \cdot \nabla \boldsymbol{w}^1}{\mu_f \nabla^2 \boldsymbol{w}^1} \right| = O(a V_T / \nu_f) = O(Re_T),$$

$$\left| \frac{2\,\rho_f \Omega \boldsymbol{e}_3 \times \boldsymbol{w}^1}{\mu_f \nabla^2 \boldsymbol{w}^1} \right| = O(a^2 \Omega / \nu_f) = O(Ta).$$

where Re_H, Re_T and $Ta = 9\,S$ are the non-dimensional numbers introduced in § 2. Also, the time scale of the the unsteady term $\partial \boldsymbol{w}^1 / \partial t$ is $1/(\lambda^0\,\Omega)$, and we are led to

$$\left| \rho_f \frac{\partial \boldsymbol{w}^1 / \partial t}{\mu_f \nabla^2 \boldsymbol{w}^1} \right| = O\left(\frac{a^2\,\Omega\,\lambda^0}{\nu_f} \right) = O(S^2).$$

In the framework of our experiments, all these non-dimensional numbers are smaller than unity (see (2.2)). The fluid motion equation near the particle is therefore the steady Stokes equation.

In contrast, at large distances from the sphere, these terms may balance the viscous term. These distances scale, respectively, as a/Re_H, a/Re_T, $a/\sqrt{Ta}$ (Ekman length) and a/S. Provided

$$Ta \gg Re_T^2, \quad Ta \gg Re_H^2, \quad Ta \gg S^2,$$

the convective Coriolis term can be taken into account at the expense of the three other terms. In our experiments, these three conditions are satisfied (see table 1). Accordingly, the far-off velocity field satisfies approximately

$$\rho_f(2\Omega \boldsymbol{e}_3 \times \boldsymbol{w}^1) = -\nabla \widehat{P}^1 + \mu_f \nabla^2 \boldsymbol{w}^1. \tag{3.21}$$

Then we recover the problem considered by Herron *et al.* (1975) (see also Miyazaki 1995), which can be solved by using classical matched asymptotic expansions.

Finally, the hydrodynamic force experienced by the particle can be obtained from the three contributions of the ansatz (3.9):

$$\boldsymbol{F} = \int_S \boldsymbol{\Sigma}^0 \boldsymbol{n}\, \mathrm{d}S + \int_S \boldsymbol{\Sigma}^c \boldsymbol{n}\, \mathrm{d}S + \int_S \boldsymbol{\Sigma}^1 \boldsymbol{n}\, \mathrm{d}S = \boldsymbol{F}^0 + \boldsymbol{F}^c + \boldsymbol{F}^1,$$

where $\boldsymbol{F}^0$, $\boldsymbol{F}^c$ and $\boldsymbol{F}^1$ correspond to $\boldsymbol{\Sigma}^0$, $\boldsymbol{\Sigma}^c$ and $\boldsymbol{\Sigma}^1$ which are the stress tensors corresponding to $\boldsymbol{w}^0$, $\boldsymbol{w}^c$ and $\boldsymbol{w}^1$, respectively. $\boldsymbol{n}$ is the outward unit normal to the particle's surface. The contribution of the unperturbed velocity field ($\boldsymbol{w}^0$) is readily obtained,

$$\boldsymbol{F}^0 = \int_{\mathscr{V}} \rho_f \left(\frac{\mathrm{D}\boldsymbol{V}_f^0}{\mathrm{D}t} - \boldsymbol{g} \right) \mathrm{d}\mathscr{V}.$$

(The velocity $\boldsymbol{V}_f^0$ is the fluid velocity in the laboratory reference frame.) The contribution of the second integral is obtained by making use of the results of Childress (1964). Since in our experiments $Ta \gg Re_T^2$, this force reads

$$\boldsymbol{F}^c = -6\pi\mu_f a \left(1 + \left(\frac{a^2\Omega}{\nu_f} \right)^{1/2} \frac{4}{7} \right) V_T \boldsymbol{e}_3. \tag{3.22}$$

The contribution of $\boldsymbol{w}^1$ leads to (Herron *et al.*):

$$\boldsymbol{F}^1 = -6\pi\mu_f a \left(\boldsymbol{I} + \left(\frac{a^2\Omega}{\nu_f} \right)^{1/2} \boldsymbol{\Delta} \right) \boldsymbol{P}_H \left(\boldsymbol{V}_p - \boldsymbol{V}_f^0 \right), \tag{3.23}$$

where the mobility tensor $\boldsymbol{\Delta}$ reads

$$\boldsymbol{\Delta} = \begin{pmatrix} \Delta_{11} & -\Delta_{21} \\ \Delta_{21} & \Delta_{11} \end{pmatrix},$$

with $\Delta_{11} = 5/7$ and $\Delta_{21} = 3/5$. The diagonal components of this mobility tensor correspond to a drag increase due to the effect of the Coriolis force on the far-off perturbed velocity. The antisymmetric part of $\boldsymbol{\Delta}$ corresponds to a lift force proportional to $\boldsymbol{\Omega} \times (\boldsymbol{V}_p - \boldsymbol{V}_f^0)$. Note that Herron *et al.* (1975) also obtained the component $\Delta_{33} = 4/7$, in agreement with Childress' result. Nevertheless, the general form of Childress' result also enables us to cope with smaller rotation rates ($Ta \simeq Re_T^2$).

The hydrodynamic forces $\boldsymbol{F}^c$ and $\boldsymbol{F}^1$ have been obtained by writing the fluid motion equation in the rotating frame. This choice is very convenient since the problem is quasi-steady there. Nevertheless, in the laboratory reference frame, the fluid motion equations are unsteady, and a history term could appear in the resulting hydrodynamic force. Indeed, the equation of the perturbed velocity field $\boldsymbol{W}^1$ in the

non-rotating reference frame translating with the particle reads (see Maxey & Riley 1983):

$$\underbrace{\rho_f \frac{\partial \boldsymbol{W}^1}{\partial t}}_{\text{(i)}} + \underbrace{\rho_f(\boldsymbol{W}^1\cdot\nabla)\boldsymbol{W}^0 + \rho_f(\boldsymbol{W}^0\cdot\nabla)\boldsymbol{W}^1}_{\text{(ii)}} + \rho_f(\boldsymbol{W}^1\cdot\nabla)\boldsymbol{W}^1 = -\nabla P^1 + \mu_f \Delta \boldsymbol{W}^1, \tag{3.24}$$

where $\boldsymbol{W}^0$ is the unperturbed velocity. Since the angular velocity of the particle is very close to Ω, we can check that the boundary condition satisfied by $\boldsymbol{W}^1$ at the particle surface reads

$$\boldsymbol{W}^1 = \dot{r}(t)(\cos\Omega\, t\, \boldsymbol{e}_1 + \sin\Omega\, t\, \boldsymbol{e}_2). \tag{3.25}$$

The time scale of $\dot{r}$ is about $1/(\lambda^0\,\Omega)$ and is very large compared to $1/\Omega$. Therefore, the time scale of $\partial\boldsymbol{W}^1/\partial t$ is $1/\Omega$; the unsteady term in the fluid motion equation cannot be neglected in this reference frame. Indeed, near the inclusion, we have

$$\left|\frac{\rho_f \partial \boldsymbol{W}^1/\partial t}{\mu_f \Delta \boldsymbol{W}^1}\right| \sim \left|\frac{\rho_f(\boldsymbol{W}^1\cdot\nabla)\boldsymbol{W}^0}{\mu_f \Delta \boldsymbol{W}^1}\right| \sim \left|\frac{\rho_f(\boldsymbol{W}^0\cdot\nabla)\boldsymbol{W}^1}{\mu_f \Delta \boldsymbol{W}^1}\right| = O(Ta),$$

and the last term of the left-hand side of (3.24) scales like the particle Reynolds number and can be neglected in the framework of our experiments. Since $\boldsymbol{W}^1$ satisfies an oscillating boundary condition with time scale $1/\Omega$, the penetration depth of the perturbed velocity is of the order of $(\sqrt{\nu_f/\Omega})$, like the Ekman distance $(a/\sqrt{Ta})$ where (ii) is expected to balance the viscous term. In the following, we conjecture that (3.24) is mainly unsteady, since the perturbed flow is almost entirely contained within an inner zone affected by the particle oscillations. Note that, as shown by Coimbra & Kobayashi (2002), the convective term (ii) induces a lift force in the particle motion equation. Nevertheless, this lift force has very little effect on the radial migration of the particle in a vertical centrifuge for the values of angular rotation under study (see Candelier *et al.* 2004). Accordingly, we approximate (3.24) by the unsteady Stokes equation, and the resulting horizontal hydrodynamic force is given by the well-known BBO equation,

$$\begin{aligned}\boldsymbol{F}^1 = &-\tfrac{1}{2}m_f \frac{\mathrm{d}}{\mathrm{d}t}\left(\boldsymbol{P}_H\left(\boldsymbol{V}_p - \boldsymbol{V}_f^0\right)\right) - 6\pi\mu_f a\left(\boldsymbol{P}_H\left(\boldsymbol{V}_p - \boldsymbol{V}_f^0\right)\right)\\ &- 6a^2\sqrt{\pi\mu_f\rho_f}\int_0^t \frac{\mathrm{d}}{\mathrm{d}\tau}\left(\boldsymbol{P}_H\left(\boldsymbol{V}_p - \boldsymbol{V}_f^0\right)\right)\frac{1}{\sqrt{t-\tau}}\mathrm{d}\tau,\end{aligned} \tag{3.26}$$

where $m_f = m_p/\gamma$.

We therefore observe that by writing the fluid motion equation in the non-rotating reference frame we are led to (3.26), whereas by writing the fluid motion equation in the rotating frame and neglecting (ii) we are led to (3.23). These apparently contradictory results show that the effect of the unsteadiness of the perturbed flow observed in the former reference frame mainly corresponds to Coriolis effects on the perturbed flow in the latter. This point will be discussed below.

In the next section, the motion equation (1.1) of the particle is solved. Both the force (3.26) and the force (3.23) will be used and compared to experiments. Before that, results of the present subsection are generalized to fluid inclusions.

3.2. *Motion equation of fluid inclusions*

In order to derive the motion equations of fluid inclusions, we come back to the rotating frame and apply the same method as above. The ansatz (3.9) is replaced by

$$\boldsymbol{w}_f = \boldsymbol{w}^0 + \boldsymbol{w}^c + \boldsymbol{w}^1, \tag{3.27}$$

outside the inclusion, and:

$$\widetilde{\boldsymbol{w}}_f = \widetilde{\boldsymbol{w}}^0 + \widetilde{\boldsymbol{w}}^c + \widetilde{\boldsymbol{w}}^1, \tag{3.28}$$

inside the inclusion. The same kind of ansatz is used for the pressure field. The terms $\boldsymbol{w}^0$ and $\widetilde{\boldsymbol{w}}^0$ correspond to the horizontal unperturbed flow and are equal to $-\boldsymbol{P}_H \boldsymbol{v}_p(t)$. The terms $\boldsymbol{w}^c$ and $\widetilde{\boldsymbol{w}}^c$ are the counterpart of the term $\boldsymbol{w}^c$ of the solid particle case, and satisfy the motion equation of a fluid inclusion moving steadily along a vertical axis in a rotating flow. This problem has not been solved so far, but the hydrodynamic force corresponding to this velocity field can be obtained by generalizing Childress' approach, as suggested by Legendre & Magnaudet (1997) and Magnaudet (2003). Indeed, Childress has shown that one can take rotation-induced inertia effects into account by matching the inner Stokes solution to a uniform outer velocity field depending on the angular velocity Ω. In the external problem of this matched asymptotic approach, the inclusion is treated as a point force source term of the form $\boldsymbol{f}\delta(\boldsymbol{x})$ (δ is Dirac's delta function) added into the Navier–Stokes equations. To leading order, $\boldsymbol{f}$ is the opposite of the drag obtained in the creeping-flow approximation by Hadamard-Ribczynski (Clift, Grace & Weber 1978), $\boldsymbol{f} = 2\pi R_\mu a \mu_f V_T \boldsymbol{e}_3$, where

$$R_\mu = \frac{3+2\kappa}{1+\kappa}, \quad \kappa = \frac{\mu_f}{\mu_p}.$$

Since the external velocity field obtained by Childress is a linear function of $\boldsymbol{f}$, the outer velocity field in the case of fluid inclusions can be obtained by multiplying Childress' solution by $R_\mu/3$. Therefore, the Stokes flow around the inclusion is set to match the modified outer flow, that is $-V_T(1 + \frac{1}{3}R_\mu \frac{4}{7}(a^2\Omega/\nu_f)^{1/2})\boldsymbol{e}_3$. The corresponding hydrodynamic force acting on the inclusion is therefore

$$\boldsymbol{F}^c = -2\pi R_\mu a \mu_f V_T \left(1 + \tfrac{1}{3}R_\mu \tfrac{4}{7}\left(\frac{a^2\Omega}{\nu_f}\right)^{1/2}\right)\boldsymbol{e}_3, \tag{3.29}$$

and generalizes (3.22) to the case of fluid inclusions. Note that when $R_\mu \to 3$ (solid particles), we recover (3.22) as expected.

Note that when $\alpha = 18\,S/Re_T^2 \to 0$ (non-rotating cylinder), the generalization of Childress'results leads to

$$\boldsymbol{F}^c = -2\pi R_\mu a \mu_f V_T \left(1 + \tfrac{1}{8}R_\mu Re_T\right)\boldsymbol{e}_3. \tag{3.30}$$

If, in addition $R_\mu \to 3$, we recover the well-known Oseen correction for solid spheres. Therefore, equation (3.30) generalizes Oseen's correction to fluid inclusions of arbitrary viscosity ratios.

The motion equations of fluid inclusions in the horizontal plane can be obtained by injecting the ansatz (3.27)–(3.28) into the two-fluid mass and momentum equations of $\boldsymbol{w}_f$ and $\widetilde{\boldsymbol{w}}_f$, together with the appropriate boundary conditions at the fluid–fluid interface and at infinity. For the same reasons as in the solid sphere case, the unsteady term can be neglected, and we are led to the steady Stokes equation, with a Coriolis source term, for $\boldsymbol{w}^1$ and $\widetilde{\boldsymbol{w}}^1$. The matched asymptotic procedure used by Herron *et al.*

can be generalized to fluid inclusions as described above, and we are led to

$$\boldsymbol{F}^1 = -2\pi\mu_f a\, R_\mu \left(\boldsymbol{I} + \tfrac{1}{3} R_\mu \left(\frac{a^2\Omega}{\nu_f} \right)^{1/2} \boldsymbol{\Delta} \right) \boldsymbol{P}_H \left(\boldsymbol{V}_p - \boldsymbol{V}_f^0 \right). \tag{3.31}$$

Also, as for solid spheres, we note that by writing the fluid motion equations in the laboratory reference frame rather than in the rotating frame, and assuming the horizontal contribution of inertia effects can be neglected, we obtain (see Gorodtsov 1975; Yang & Leal 1991; Galindo & Gerbeth 1993):

$$\begin{aligned} \boldsymbol{F}^1(t) = -\tfrac{1}{2} m_f \frac{\mathrm{d}}{\mathrm{d}t} \left(\boldsymbol{P}_H \left(\boldsymbol{V}_p(t) - \boldsymbol{V}_f^0 \right) \right) - 2\pi a \mu_f R_\mu \left(\boldsymbol{P}_H \left(\boldsymbol{V}_p(t) - \boldsymbol{V}_f^0 \right) \right) \\ - 2\pi a \mu_f \int_{-\infty}^{t} K(t-\tau) \frac{\mathrm{d}}{\mathrm{d}\tau} \left(\boldsymbol{P}_H \left(\boldsymbol{V}_p(\tau) - \boldsymbol{V}_f^0 \right) \right) \mathrm{d}\tau, \end{aligned} \tag{3.32}$$

where the kernel of the history force has a very complicated expression in the general case. For bubbles we have $\mu_p/\mu_f \ll 1$, so that we can show that the kernel is (Gorodtsov 1975): $K(t) = 4\exp(9\nu_f t/a^2)\mathrm{erfc}(\sqrt{9\nu_f t/a^2})$.

To conclude this whole section, the motion equation of solid or gaseous inclusions reads

$$m_p \frac{\mathrm{d}^2 \boldsymbol{X}_p}{\mathrm{d}t^2} = m_p \boldsymbol{g} + \boldsymbol{F}^0 + \boldsymbol{F}^c + \boldsymbol{F}^1, \tag{3.33}$$

where $\boldsymbol{F}^0$, $\boldsymbol{F}^c$ and $\boldsymbol{F}^1$ are given by the various expressions obtained in this section. In the following, equation (3.33), together with the initial conditions

$$\boldsymbol{X}_p(0) = \boldsymbol{X}_{p0}, \quad \frac{\mathrm{d}\boldsymbol{X}_p}{\mathrm{d}t}(0) = V_T\, \boldsymbol{e}_3 + \boldsymbol{V}_f^0(\boldsymbol{X}_{p0}),$$

is solved analytically and the resulting trajectories are compared to experiments. Since the vertical speed is constant and totally uncoupled from the horizontal motion, the vertical projection of (3.33) can be solved separately to obtain the terminal velocity V_T. The radial motion is investigated in § 5. Note that we can argue that the initial horizontal slip velocity is non-zero when the particle is released in our experiments, and this is in contradiction to the initial conditions above. Nevertheless, we define the time $t = 0$ as the time when the particle has reached its terminal vertical velocity, that is a few seconds after the particle release. At that time, the radial slip velocity is still very small, so that the initial conditions stated above are approximately valid.

For the sake of simplicity, the time $t = 0$ shown on the experimental curves below corresponds to the time when the particle reaches the test area (see figure 1).

Note also that the hydrodynamic forces obtained in this section are valid in a fluid of infinite extent. Therefore, the comparison between experiments and theories will have to be done with care (see below).

4. Terminal vertical velocity

We now confine attention to the prediction of the terminal velocity V_T. By writing that the vertical drag (3.29) balances the buoyancy we are led to:

$$\frac{V_T}{V_T^{\mathrm{Stokes}}} \simeq \frac{1}{1 + \frac{4}{7} R_\mu \sqrt{S}}, \tag{4.1}$$

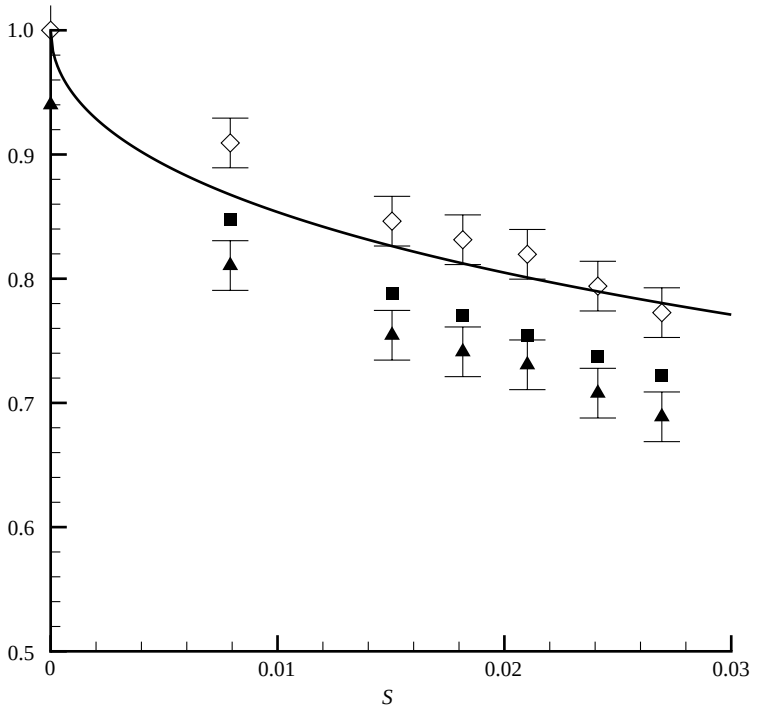

FIGURE 8. Plot of the terminal velocity V_T of a solid sphere *vs.* the Stokes number. Solid line, equation (4.1); ▲, V_T/V_T^{Stokes} (our experiments); ■, V_T/V_T^{Stokes} (experimental data interpolated from Maxworthy 1965); ◇, V_T/V_T^0, where V_T^0 is the experimental terminal velocity of the sphere when $\Omega = 0$. The terminal Reynolds number Re_T ranges from 0.1 (when $S = 0$) to 0.06 (when $S = 0.03$). The horizontal Reynolds number Re_H ranges from 0 (when $S = 0$) to 0.03 (when $S = 0.03$).

where V_T^{Stokes} denotes the terminal velocity of either solid or fluid inclusions, obtained when all inertia effects are neglected, namely:

$$V_T^{\text{Stokes}} = \tfrac{2}{3}\frac{a^2(1-\gamma)g}{R_\mu \nu_f},$$

and γ is the density ratio. In our solid particle experiments, the smallest non-zero α is about 20, so that (4.1) is valid. Also, the typical value of α for the bubbles considered in our experiments is about 6 (see table 1), and this is sufficient for the approximation (4.1) to be valid (see Childress 1964).

4.1. *Comparison with experiments*

As noted in § 2, the vertical velocity of the inclusions is constant for the time range considered in our experiments. Figures 8 and 9 show this terminal velocity versus S for the two kinds of inclusion.

Figure 8 shows the experimental and theoretical values of V_T/V_T^{Stokes} versus the Stokes number, for solid particles. Also, an interpolation of Maxworthy's experimental data (Maxworthy 1965) with the same ratio a/R, is plotted on the same graph for comparison. These two curves agree rather well, but both are below the theoretical curve (4.1). This might be due to a wall effect. Indeed, for viscous flows, the spatial decay of the perturbed velocity profile is rather slow, so that walls must be taken

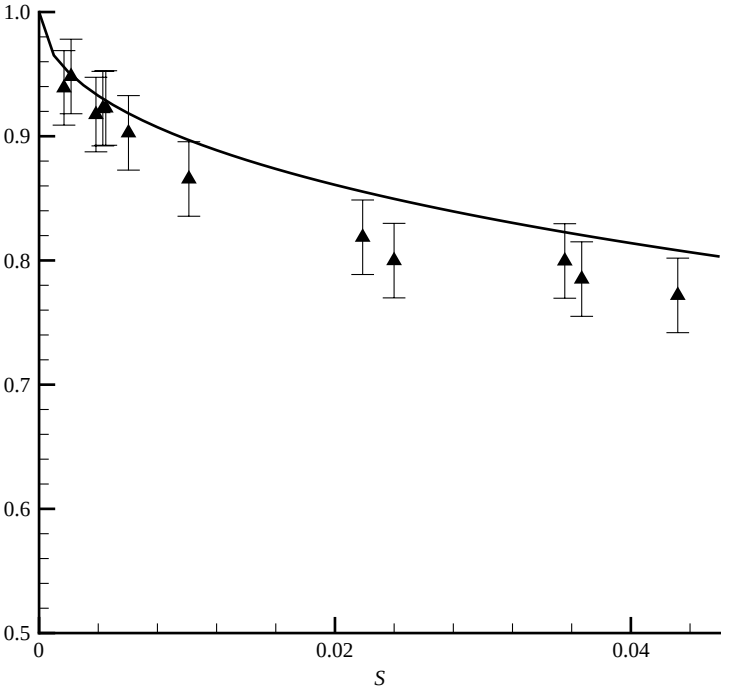

FIGURE 9. Plot of the terminal velocity of bubbles *vs.* the Stokes number. Solid line, equation (4.1); ▲, V_T/V_T^{Stokes} (our experiments). The terminal Reynolds number Re_T ranges from 0.1 to 0.3. The horizontal Reynolds number Re_H ranges from 0 to 0.08.

into account for efficient predictions. As shown by Happel & Brenner (1983) in the non-rotating case, walls affect the terminal velocity via a multiplicative factor of the form $1 + ca/R$, where $c \approx 2.1$ is almost constant on a wide part of the cross-section. Therefore, the terminal velocity, say V_T^0, of a particle dropped in our tank at rest should be independent of its radial location, provided it is not too close to the wall, i.e. $R - r$ is larger than a few particle radii. (We have checked this carefully and observed a good agreement between Happel & Brenner's theory and our measurements.) We believe that in the rotating case the terminal velocity V_T should be compared to V_T^0 instead of V_T^{Stokes} since V_T^{Stokes} corresponds to a wall-free theory.

Indeed, in the rotating case, the particle migrates in the radial direction and this radial motion does not affect the terminal vertical velocity (as we noticed, for example, in figures 4 and 6*a*). This suggests that wall effects in the rotating case are also constant on a large part of the cross-section. Assuming that these wall effects are manifested by a multiplicative factor independent of Ω, the ratio V_T/V_T^0 should be equal to the theoretical (wall-free) ratio V_T/V_T^{Stokes} given by (4.1) (since wall effects would cancel out in V_T/V_T^0). The diamond curve of figure 8 tends to confirm this conjecture, since it is close to the theoretical wall-free ratio V_T/V_T^{Stokes} (solid line).

Figure 9 shows the experimental and theoretical values of V_T/V_T^{Stokes} for bubbles. As for solid spheres, the experimental V_T/V_T^{Stokes} is smaller than the theoretical prediction, because of wall effects. In contrast with solid spheres, the velocity of the bubble in the absence of rotation V_T^0 is unknown, since each bubble is lost once it reaches the top of the cylinder (and we cannot produce two bubbles with exactly the same radius). Hence, we cannot check whether V_T/V_T^0 agrees with (4.1). Nevertheless,

we observe that wall effects are slightly less significant for bubbles. This might be due to the length-scale of the flow induced by the inclusion being smaller for bubbles than for solid spheres. Indeed, the reflections method used by Happel & Brenner (1983) for solid spheres can be generalized to fluid inclusions (in the same way as inertia effects). By using this approach, we can show that the terminal velocity of fluid inclusions in a still cylindrical tank is $V_T^{\mathrm{Stokes}}/(1+(R_\mu/3)ca/R)$, where c is the same as for solid inclusions (i.e. $c \approx 2.1$). This should explain why our measurements are slightly closer to the wall-free theory for bubbles ($R_\mu = 2$) than for solid particles ($R_\mu = 3$).

Finally, the experimental results discussed in this section show that the terminal velocity of either solid or gaseous inclusions is affected by the rotation of the fluid via an inertial effect due to the Coriolis force. By neglecting this inertial effect, one would overestimate the terminal velocity of more than 20 % as soon as the Stokes number is larger than 0.03.

5. Radial migration of the inclusion

5.1. *Theoretical trajectories*

The motion equation of the inclusion in the horizontal plane ($\boldsymbol{e}_1, \boldsymbol{e}_2$) is obtained from the horizontal projection of (3.33):

$$m_p \frac{\mathrm{d}^2 \boldsymbol{X}_p}{\mathrm{d}t^2} = m_f \frac{\mathrm{D}\boldsymbol{V}_f^0}{\mathrm{D}t} + \boldsymbol{F}^1,$$

where $\boldsymbol{F}^1$ is given by (3.31) or by (3.32) according to whether the fluid motion equations have been written in the rotating or non-rotating reference frame. As discussed above, these two expressions should lead to similar particle trajectories. The goal of this section is to confirm this point theoretically and experimentally. The motion equation is solved by introducing the complex position

$$Z(t) = \boldsymbol{X}_p(t)\cdot\boldsymbol{e}_1 + \mathrm{i}\boldsymbol{X}_p(t)\cdot\boldsymbol{e}_2 \qquad (\mathrm{i}^2 = -1),$$

in terms of which the particle motion equation reads

$$\ddot{Z} = -\frac{Z}{\gamma} + \frac{R_\mu}{6S\gamma}\left(1 + R_\mu \Delta_{11} S^{1/2}\right)(\mathrm{i}Z - \dot{Z}) - \frac{R_\mu^2}{6S^{1/2}\gamma}\Delta_{12}(Z + \mathrm{i}\dot{Z}) \tag{5.1}$$

by using (3.31), or

$$\ddot{Z} + \mathrm{A}\dot{Z} + \mathrm{B}Z + \mathrm{C}\int_0^t (-\ddot{Z}(\tau) + \mathrm{i}\dot{Z}(\tau))\mathscr{K}((t-\tau)/S)\,\mathrm{d}\tau = 0, \tag{5.2}$$

by using (3.32). In these equations, lengths and times have been normalized by the cylinder radius R and by $1/\Omega$. The constants A, B and C depend only on S and γ and are given in Appendix A. Equation (5.1) is readily solved, and equation (5.2) is solved by making use of Laplace transforms (see Appendix A and Candelier *et al.* 2004). Both equations predict an exponential evolution for $Z(t)$, of the form

$$Z(t) \approx Z(0)\exp(\lambda_r t)\exp(\mathrm{i}\lambda_i t) + O(S). \tag{5.3}$$

The migration rate λ_r reads, after some algebra,

$$\frac{\dot{r}}{r} = \lambda_r = \frac{6}{R_\mu} S(\gamma - 1) - 6\,\Delta_{11} S^{3/2}(\gamma - 1) + O(\Delta_{12}\, S^2) \tag{5.4}$$

if we solve (5.1) and

$$\frac{\dot{r}}{r} = \lambda_r = \frac{6}{R_\mu} S(\gamma - 1) - 3\sqrt{2} S^{3/2}(\gamma - 1) + O(S^2) \tag{5.5}$$

if we solve (5.2). These two expressions are very close since $3\sqrt{2} \simeq 4.24$ and $6\,\Delta_{11} \simeq 4.28$, in agreement with the fact that the two approaches discussed above (i.e. the fluid motion equation written in the rotating frame and the fluid motion equation written in the non-rotating frame) describe the same physical phenomenon.

These results are valid for both solid spheres ($R_\mu = 3$) and bubbles ($R_\mu = 2$). For solid spheres, (5.5) has already been derived by Candelier *et al.* (2004), and coincides with that of Druzhinin & Ostrovsky (1994) obtained with a different asymptotic approach, and for a purely two-dimensional motion. The rotation rate reads

$$\dot{\theta} = \lambda_i = 1 - 6\,\Delta_{12} S^{3/2}(\gamma - 1) + O(S^2) \tag{5.6}$$

if we solve (5.1) and

$$\dot{\theta} = \lambda_i = 1 - 3\sqrt{2}\, S^{3/2}(\gamma - 1) + O(S^2) \tag{5.7}$$

if we solve (5.2). There is a sensitive difference between the $O(S^{3/2})$ terms appearing in the two λ_i, since $3\sqrt{2} \simeq 4.24$ and $6\,\Delta_{12} = 3.60$. This might be because the term (ii) has been neglected in (3.24), so that a possible additional lift force is missing in the particle motion equation (5.2). Candelier *et al.* (2004) have shown that by adding a lift force of the form $C\,\Omega \boldsymbol{e}_3 \times \boldsymbol{V}_g$ into the BBO equation, one modifies the $O(S^{3/2})$ term of (5.7). In particular, we have checked this way that Saffman's lift force leads to an overestimated azimuthal slip velocity. This confirms that Saffman's lift is not appropriate here. Note, however, that the contribution of this $S^{3/2}$ term cannot be verified experimentally since it is much smaller than the leading-order term $\lambda_i = 1$. Note also that R_μ does not appear in the rotation rate λ_i: it is only sensitive to the density ratio γ.

All the $S^{3/2}$ contributions appearing in these formulae manifest Coriolis or history effects. Note that even though the kernel is very different for solid and fluid inclusions, the absolute contribution to the migration and rotation rate is the same for these two kinds of inclusion, since R_μ does not appear in the $O(S^{3/2})$ term. Nevertheless, solid particles are more sensitive to these effects than fluid inclusions, since the ratio of the $O(S^{3/2})$ term to the $O(S)$ term is larger for solid inclusions. In the following, positive λ_r are denoted 'ejection rates' and correspond to solid particles with $\gamma > 1$, and negative λ_r are denoted 'trapping rates' ($\gamma < 1$).

5.2. *Comparison with experiments*

Figures 10 and 11 show the experimental and theoretical values of the ejection or trapping rate λ_r for solid spheres and bubbles, obtained from the slope of the curve $\ln r(t)$ versus t (see, for example, figure 7). For solid spheres, the experiments are reproducible as we used the same inclusion for our measurements. Therefore, for each Stokes number, the experimental ejection rate is averaged over several runs, and is characterized by very small fluctuations around its mean value. In contrast, in spite of the elaborated bubble injection device, we cannot use the same bubble twice. Therefore, the trapping rate of bubbles shown in figure 11 is not an averaged value. Nevertheless, the uncertainty about the trapping rate remains small compared to the uncertainty about the radius, and consequently about the Stokes number. This is the reason why the horizontal error bars remain rather large in figure 11. However, the experiment remains conclusive for the two kinds of inclusion.

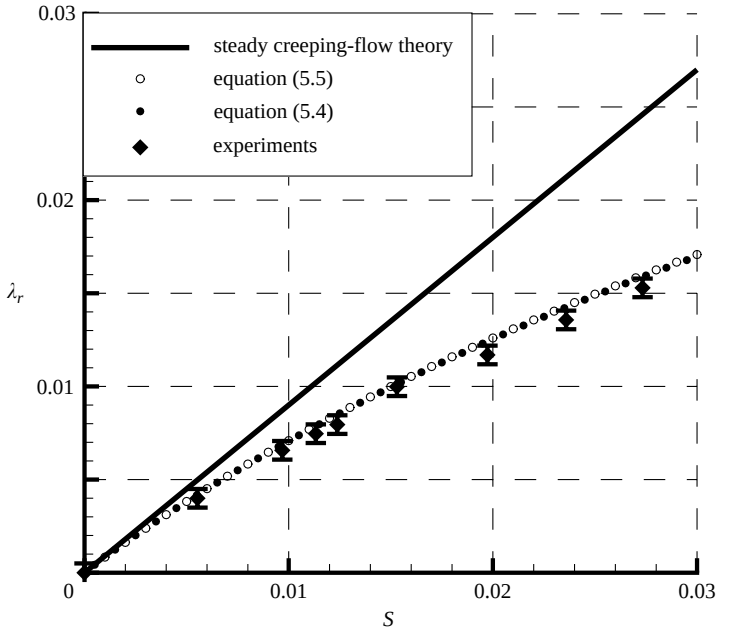

FIGURE 10. Non-dimensional ejection rate of a solid particle *vs.* the Stokes number.

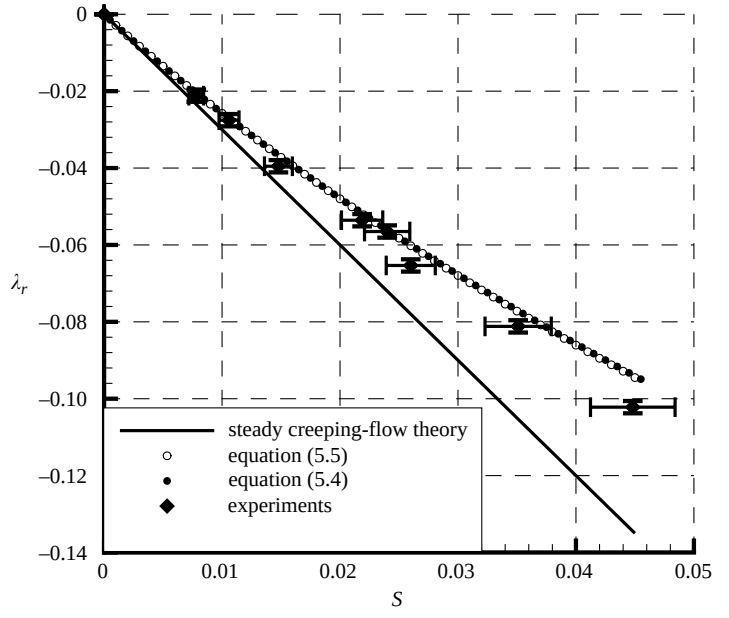

FIGURE 11. Non-dimensional trapping rate of a bubble *vs.* the Stokes number.

For solid spheres we recover the results of Candelier *et al.* (2004). For fluid inclusions, (5.5) and (5.7) generalize their results and we observe that the theoretical trapping rate (5.5) agrees with our measurements. Moreover, as noted above, the results (5.4) and (5.5) are undistinguishable, for either solid or gaseous inclusions.

In contrast, the $S^{3/2}$ term of the rotation rate cannot be measured experimentally because its contribution is too weak compared to unity. Nevertheless, we can see that both (5.6) and (5.7) predict that inclusions lighter than the fluid will rotate faster than the tank (since $\gamma - 1 < 0$ there). We have indeed observed this effect for bubbles, even though we could not measure it accurately (the $S^{3/2}$ term is smaller than our experimental uncertainty about λ_i). As for the terminal velocity, the physical interpretation of these results will be discussed below.

6. Discussion and conclusion

6.1. *General considerations*

The experiments presented in this paper suggest that the trajectories of either gaseous or solid inclusions within the vortex are sensitive to both inertia effects and history effects. Assuming that the vertical velocity of the inclusion is constant after a short transient (as suggested by experiments), the fluid motion equations around the inclusion show that inertia effects must be taken into account to predict the vertical terminal velocity. For solid particles, we are led to Childress' equation to predict the terminal velocity, even if the particle experiences a radial migration. For fluid inclusions, we have generalized Childress' equation as suggested by Legendre & Magnaudet (1997) and Magnaudet (2003).

The horizontal motion of the particle has also been investigated. By writing the fluid motion equations in the rotating frame, we are led to a quasi-steady equation for the perturbed velocity where the Coriolis force has to be taken into account. This induces drag corrections as well as a lift force in the particle motion equation (Herron *et al.* 1975). In particular, these drag corrections significantly reduce the migration rate of the particle. By writing the fluid motion equations in the laboratory reference frame, we are led to an unsteady equation for the perturbation velocity and, if we remove the convective terms in this unsteady equation, to a Basset-like history force in the particle motion equation. Even though both approaches lead to different expressions for the hydrodynamic force experienced by the inclusion, they lead to almost undistinguishable particle trajectories.

An experimental device has been built to check these theories. It consists in a rotating closed cylinder filled with silicone oil, in which inclusions (either fluid or solid) are injected and followed with a mobile camera. For bubbles, an elaborate injector device has been designed. We have chosen to confine attention to both the terminal velocity V_T and the radial migration and rotation rates (λ_r, λ_i) since these quantities can be carried out analytically and experimentally, and contain rich dynamical information.

Our experimental results concerning the vertical speed of solid spheres agree with Childress' theoretical predictions (Childress 1964), and corroborate the experimental analyses of Maxworthy (1965). In particular, rotation-induced inertia effects (manifested by the Coriolis term in the fluid motion equation) decrease the terminal velocity down to 20 %, for the Stokes numbers considered here. As for fluid inclusions, a similar effect is observed. The agreement between experiments and the generalized Childress theory is satisfactory.

As far as the radial migration is concerned, the theoretical migration rates λ_r given by either (5.4) or (5.5) have been confirmed experimentally. Even if the two expressions for $\boldsymbol{F}^1$, namely (3.23) and (3.26), are different, we can show that they are nearly equivalent in this problem. Indeed, if we neglect the time dependence of $\dot{r}(t)$ in the boundary condition (3.25), the unsteady Stokes problem reduces to the

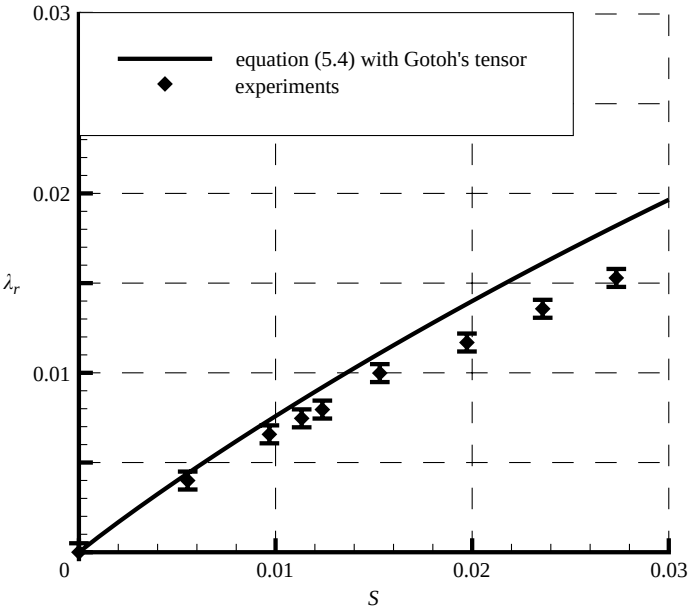

FIGURE 12. Non-dimensional ejection rate of a solid particle *vs.* the Stokes number predicted by using Gotoh's mobility tensor.

superposition of two single-frequency oscillations (along $\boldsymbol{e}_1$ and $\boldsymbol{e}_2$), and the history integral in the particle motion equation, say $\boldsymbol{F}_h$, can be solved (see for example; Landau & Lifchitz 1989; Coimbra & Rangel 2001), and reads

$$\boldsymbol{F}_h \simeq -6\pi\mu_f a \left(\frac{a^2\Omega}{\nu_f}\right)^{1/2} \begin{pmatrix} \sqrt{2}/2 & -\sqrt{2}/2 \\ \sqrt{2}/2 & \sqrt{2}/2 \end{pmatrix} \boldsymbol{P}_H(\boldsymbol{V}_p - \boldsymbol{V}_f^0).$$

The diagonal of this mobility tensor is very close to that of Herron *et al.* since, once again, $\sqrt{2}/2 \simeq 0.707$ and $5/7 \simeq 0.714$. As noted above, this shows that the effect of the unsteadiness of the perturbed flow observed in the non-rotating reference frame might correspond to Coriolis effects on the perturbed flow in the rotating reference frame. Note also that some discrepancies appear in the non-diagonal components and this might be because the term (ii) in the fluid motion equation in the non-rotating frame, responsible for a lift effect (see Coimbra & Kobayashi 2002), has been neglected.

Because of the unsteadiness of boundary condition (3.25), we cannot neglect the unsteady term $\partial \boldsymbol{W}^1/\partial t$ in equation (3.24) and keep the $O(Ta)$ convective terms. Therefore, the mobility tensor of Gotoh (1990) is not expected to give satisfactory results here. Nevertheless, since this tensor is close to that of Herron *et al.* (1975), we have solved the particle motion equation predicted with Gotoh's mobility tensor, and obtained an analytical expression for the migration rate λ_r (simply replace $\Delta_{11} = 5/7$ by $\Delta_{11} = (3\sqrt{2}/280)(19 + 9\sqrt{3})$ in equation (5.4)). Figure 12 shows the migration rate predicted by Gotoh's theory, together with experimental points. As expected, the agreement is not as good as that obtained with the Boussinesq–Basset force (open circles in figure 10).

Even if the mobility tensor of Gotoh and that of Herron *et al.* lead to different results in our problem, there is no contradiction here, since the problem is unsteady in the laboratory reference frame and quasi-steady in the rotating frame. (This point

has been discussed in detail by Miyazaki 1995.) In the present problem, both our theoretical and experimental analyses show that the theory of Herron *et al.* (1975) (obtained by writing the fluid motion equation in the rotating frame) agrees with the BBO equation (obtained by writing the fluid motion equation in the non-rotating frame and neglecting the horizonal contribution of inertia terms) rather than with Gotoh's result. In contrast, the mobility tensor of Gotoh (1990) should be used for example when the particle is held fixed in the laboratory reference frame.

We are indebted to Bruno Chenu and Alain Delconte for the design and the set-up of the experimental apparatus.

Appendix A. Solution of the horizontal motion equations

In order to solve the generalized horizontal motion equation (3.32), it is convenient to re-write it in the form:

$$m_p \frac{\mathrm{d}^2 \boldsymbol{X}_p}{\mathrm{d}t^2} = m_f \frac{\mathrm{D}\boldsymbol{V}_f^0}{\mathrm{D}t} - \tfrac{1}{2} m_f \left(\boldsymbol{P}_H \frac{\mathrm{d}}{\mathrm{d}t} \boldsymbol{V}_p(t) - \frac{\mathrm{D}\boldsymbol{V}_f^0}{\mathrm{D}t} \right) - k\pi a \mu_f \left[\left(\boldsymbol{P}_H \boldsymbol{V}_p(t) - \boldsymbol{V}_f^0 \right) + C_h \int_{-\infty}^{t} \mathscr{K}\left(\frac{9\nu_f (t-\tau)}{a^2} \right) \frac{\mathrm{d}}{\mathrm{d}\tau} \left(\boldsymbol{P}_H \boldsymbol{V}_p(\tau) - \boldsymbol{V}_f^0 \right) \mathrm{d}\tau \right], \tag{A 1}$$

where the added-mass term has been changed according to Auton (1987) (see also Magnaudet *et al.* 1995). The terms k, C_h and $\mathscr{K}$ have been introduced for the sake of clarity and read

$$k = 6, \;\; C_h = 3/\sqrt{\pi}, \;\; \mathscr{K}(s) = 1/\sqrt{s}$$

for solid particles, and

$$k = 4, \;\; C_h = 2, \;\; \mathscr{K}(s) = \operatorname{erfc}(\sqrt{s}) \exp(s)$$

for fluid inclusions with $\mu_p/\mu_f \ll 1$. Note that we made use of the fact that, for the flow considered here, $\boldsymbol{P}_H \boldsymbol{V}_f^0 = \boldsymbol{V}_f^0$. In the following, (A 1) is normalized by the cylinder radius R (for lengths) and $1/\Omega$ (for times). Also, by writing:

$$Z(t) = \boldsymbol{X}_p(t) \cdot \boldsymbol{e_1} + \mathrm{i} \boldsymbol{X}_p(t) \cdot \boldsymbol{e}_2, \qquad (\mathrm{i}^2 = -1),$$

we are led to (5.2) where $\dot{Z}$ denotes $\mathrm{d}Z(t)/\mathrm{d}t$ and

$$\mathrm{A} = \frac{k}{6S(2\gamma+1)}, \quad \mathrm{B} = \frac{3 - \mathrm{i}\, k/(6S)}{2\gamma+1}, \quad \mathrm{C} = \frac{-k\, C_h}{6S(2\gamma+1)}. \tag{A 2}$$

The initial no-slip condition, in terms of the complex variable Z, reads $\dot{Z}(0) = \mathrm{i} Z(0)$.

Let $U = \dot{Z}$, so that (5.2) now becomes

$$\dot{U} + \mathrm{A}U + \mathrm{B} \left[\int_0^t U(\tau)\, \mathrm{d}\tau + Z(0) \right] + C \int_0^t (-\dot{U}(\tau) + \mathrm{i} U(\tau)) \mathscr{K}((t-\tau)/S)\, \mathrm{d}\tau = 0, \tag{A 3}$$

and can be solved by using the classical Laplace transform:

$$\widetilde{U}(p^2 + \mathrm{A}\, p + \mathrm{B} - \mathrm{C} p(p - \mathrm{i})\widetilde{K}) = U(0) p (1 - \mathrm{C}\widetilde{K}) - \mathrm{B} Z(0),$$

where $\widetilde{U}(p)$ and $\widetilde{K}(p)$ denote, respectively, the Laplace transform of $U(t)$ and $\mathscr{K}(t/S)$. For the sake of simplicity, let $X = \sqrt{p}$, so that

$$\widetilde{U} = \frac{U(0)X^2(1 - \mathrm{C}\widetilde{K}(X)) - \mathrm{B}Z(0)}{\underbrace{X^4 + \mathrm{A}\,X^2 + \mathrm{B}}_{P^0(X)} - \underbrace{\mathrm{C}\widetilde{K}(X)X^2(X^2 - \mathrm{i})}_{P^1(X)}}.$$

In this last expression, $P^0(X)$ characterizes the case without history force and $P^1(X)$ shows that the history force is present. In order to find the solution of the motion equation, $\widetilde{U}$ must be written using a partial decomposition of the form $\widetilde{U} = \sum_{i=1}^{n} A_i/(X - X_i)$, where the roots X_i of the polynomial $P_n(X) = P^0(X) + P^1(X)$ have to be found.

In the solid particle case, the constants A_i read

$$A_i = \frac{U(0)\left(X_i^2 - \mathrm{C}\sqrt{S\pi}X_i\right) - \mathrm{B}Z(0)}{\prod_{\substack{j=1 \\ j\neq i}}^{j=4} (X_i - X_j)}$$

and the polynomial is

$$P_4(X) = X^4 + \mathrm{A}X^2 + \mathrm{B} - \mathrm{C}\sqrt{\pi S}X(X^2 - \mathrm{i}).$$

In the case of bubbles, we have

$$A_i = \frac{U(0){X_i}^3 + U(0)X_i^2/\sqrt{S} - (\mathrm{C}U(0) + \mathrm{B}Z(0))X_i - \mathrm{B}Z(0)/\sqrt{S}}{\prod_{\substack{j=1 \\ j\neq i}}^{j=5} (X_i - X_j)}$$

and

$$P_5(X) = (X^4 + \mathrm{A}X^2 + \mathrm{B})(X + 1/\sqrt{S}) - \mathrm{C}X(X^2 - \mathrm{i}).$$

Inverting the Laplace transform, we finally obtain

$$Z(t) = \sum_{i=1}^{i=n} \frac{A_i}{X_i} \exp(X_i^2\, t)\mathrm{erfc}(-X_i\sqrt{t}). \tag{A 4}$$

When $\gamma = 1$, $\pm\sqrt{\mathrm{i}}$ are roots of both $P_4(X)$ and $P_5(X)$ so that these polynomials can be solved and we obtain $Z(t) = Z(0)\exp(\mathrm{i}t)$, in agreement with there being neither radial migration nor azimuthal slip in these cases. When $\gamma \neq 1$, an approximate expression is derived in Appendix B.

Appendix B. Approximate expression for the roots X_i

First, it is convenient to seek the roots of the polynomial $Q_n(X, \gamma) = P_n(X)S(2\gamma + 1)$ instead of $P_n(X)$ since this new polynomial depends linearly on γ:

$$Q_n(X) = \Pi_n^0(X) + S(\gamma - 1)\Pi_n^1(X)$$

in which $\Pi_n^0(X)$ and $\Pi_n^1(X)$ are nth-order polynomials independent of γ, and such that $\Pi_n^0(X_1^0) = \Pi_n^0(X_2^0) = 0$, where $X_1^0 = \sqrt{\mathrm{i}}$ and $X_2^0 = -\sqrt{\mathrm{i}}$. Let us now write

$$X_i = X_i^0 + \delta X_i$$

with

$$|\delta X_i| << |X_i^0|.$$

As X_i is a root of Q_n we have:

$$0 = Q_n(X_i) = \left.\frac{\partial \Pi_n^0}{\partial X}\right|_{X_i^0} \delta X_i + S(\gamma - 1)\Pi_n^1(X_i^0) + S(\gamma - 1)\left.\frac{\partial \Pi_n^1}{\partial X}\right|_{X_i^0} \delta X_i + O\left(\delta X_i^2\right).$$

Hence,

$$\delta X_i \simeq -\frac{S(\gamma - 1)\Pi_n^1\left(X_i^0\right)}{\left.\frac{\partial \Pi_n^0}{\partial X}\right|_{X_i^0} + S(\gamma - 1)\left.\frac{\partial \Pi_n^1}{\partial X}\right|_{X_i^0}}. \tag{B 1}$$

By making use of the fact that $S \ll 1$, we can check that only the roots X_1 and X_2 (located in the vicinity of $\pm\sqrt{\mathrm{i}}$) bring significant contributions into $Z(t)$ and that $X_2 = -X_1 + O(S)$. By using the classical relations between the roots of a polynomial, we obtain

$$\sum_{i=1}^{n} \frac{A_i}{X_i} = Z(0). \tag{B 2}$$

These results lead us to an approximate expression

$$Z(t) \simeq Z(0) \exp\left(X_1^2 t\right) + O(S).$$

The motion is therefore characterized by an exponential time dependence with radial migration rate $\lambda_r = \mathrm{Re}(X_1^2)$ and rotation rate $\lambda_i = \mathrm{Im}(X_1^2)$, where Re and Im denote the real and imaginary parts, respectively. The root X_1 is obtained from (B 1) in terms of S and γ, and by taking the square of X_1 we obtain the complex growth rate λ, the real part of which is given by (5.5) and the imaginary part by (5.7).

REFERENCES

Abbad, M. & Souhar, M. 2004*a* Effects of the history force on an oscillating rigid sphere at low Reynolds number. *Exps. Fluids* **36**, 775–782.

Abbad, M. & Souhar, M. 2004*b* Experimental investigation on the history force acting on oscillating fluid spheres at low Reynolds number. *Phys. Fluids* **16**, 3808–3817.

Auton, T. R. 1987 The lift force on a spherical body in rotationnal flow. *J. Fluid Mech.* **183**, 199–218.

Basset, A. B. 1888 *Treatise on Hydrodynamics,* vol. 2, pp. 285–297. Deighton Bell, London.

Boussinesq, J. 1885 Sur la résistance qu'oppose un fluide indéfini au repos sans pesanteur au mouvement varié d'une sphère solide qu'il mouille sur toute sa surface quand les vitesses restent bien continues et assez faibles pour que leurs carrés et produits soient négligeables. *C. R. Acad. Sci. Paris* **100**, 935–937.

Candelier, F., Angilella, J. R. & Souhar, M. 2004 On the effect of the Boussinesq–Basset force on the radial migration of a Stokes particle in a vortex. *Phys. Fluids* **16**, 1765–1776.

Childress, S. 1964 The slow motion of a sphere in a rotating, viscous fluid. *J. Fluid Mech.* **20**, 305–314.

Clift, R., Grace, J. R. & Weber, M. E. 1978 *Bubbles, Drops and Particles.* Academics.

Coimbra, C. F. M. & Kobayashi, M. H. 2002 On the viscous motion of a small particles in a rotating cylinder. *J. Fluid Mech.* **469**, 257–286.

Coimbra, C. F. M., L'Esperance, D., Lambert, R. A., Trolinger, J. D. & Rangel, R. H. 2004 An experimental study of stationary history effects in high-frequency Stokes flows. *J. Fluid Mech.* **504**, 353–363.

Coimbra, C. F. M. & Rangel, R. H. 1998 General solution of the particle momentum equation in unsteady flows. *J. Fluid Mech.* **370**, 53–72.

Coimbra, C. F. M. & Rangel, R. H. 2001 Spherical particle motion in harmonic Stokes flows. *AIAA J.* **39**, 1673–1682.

Druzhinin, O. A. & Ostrovsky, L. A. 1994 The influence of the Basset force on a particle dynamics in two-dimensional flows. *Physica* D **76**, 34–43.

Galindo, V. & Gerbeth, G. 1993 A note on the force on an accelerating spherical drop at low Reynolds number. *Phys. Fluids* **5**, 3290–3292.

Gorodtsov, V. A. 1975 Slow motions of a liquid drop in a viscous liquid. *Zh. Prikl. Mekh. Tekh. Fiz.* **6**, 32–37.(Trans. J. Appl. Mech. Tech. Phys. **16**, 865–868.)

Gotoh, T. 1990 Brownian motion in a rotating flow *J. Statist. Phys.* **59**, 371–402.

Happel, J. & Brenner, H. 1983 *Low Reynolds Hydrodynamics.* Kluwer.

Harper, E. Y. & Chang, I. D. 1968 Maximum dissipation resulting from lift in a slow viscous shear flow. *J. Fluid Mech.* **33**, 209–225.

Herron, I. H., Davis, S. & Bretherton F. P. 1975 On the sedimentation of a sphere in a centrifuge. *J. Fluid Mech.* **68**, 209–234.

Kaplun, S. & Lagerstrom, P. A. 1957 Asymptotic expansions of Navier–Stokes solutions for small Reynolds numbers. *J. Math. Mech.* **6**, 585–593.

Karanfilian, S. K. & Kotas, T. J. 1981 Motion of a spherical particle in a liquid rotating as a solid body. *Proc. R. Soc. Lond.* A **376**, 525–544.

Landau, L., Lifchitz, E. 1989 *Physique théorique,* vol. 6, *Mécanique des fluides* (ed. Mir), pp. 127–129.

Legendre, D. & Magnaudet, J. 1997 A note on the lift force on a spherical bubble or drop in a low-Reynolds-number shear flow. *Phys. Fluids* **9**, 3572–3574.

Legendre, D. & Magnaudet, J. 1998 The lift force on a spherical bubble in a viscous linear shear flow. *J. Fluid Mech.* **368**, 81–126.

Lovalenti, P. M. & Brady, J. F. 1993 The force on a bubble, drop or particle in arbitrary time dependent motion at small Reynolds number. *Phys. Fluids* **5**, 2104–2116.

McLaughlin, J. B. 1991 Inertial migration of a small sphere in linear shear flows. *J. Fluid Mech.* **224**, 261–274.

Magnaudet, J. 2003 Small inertial effects on a spherical bubble, drop or particle moving near a wall in a time dependent linear flow. *J. Fluid Mech.* **485**, 115–142.

Magnaudet, J., Rivero, M. & Fabre, J. 1995 Accelerated flows past a rigid sphere or a spherical bubble. Part 1. Steady straining flow. *J. Fluid Mech.* **284**, 97–135.

Maxey, M. R. & Riley, J. J. 1983 Equation of motion for a small rigid sphere in a nonuniform flow. *Phys. Fluids* **26**, 883–889.

Maxworthy, T. 1965 An experimental determination of the slow motion of a sphere in a rotating, viscous fluid. *J. Fluid Mech.* **23**, 373–384.

Mei, R. & Adrian, R. J. 1992 Flow past a sphere with an oscillation in the free-stream velocity and a unsteady drag at finite Reynolds number. *J. Fluid Mech.* **237**, 323–341.

Miyazaki, K. 1995 Dependence of the friction tensor on the rotation of a frame of reference. *Physica* A **222**, 248–260.

Miyazaki, K., Bedeaux, D., & Bonet Avalos, J. 1995 Drag on a sphere in a slow shear flow. *J. Fluid Mech.* **296**, 373–390.

Odar, F. & Hamilton, W. S. 1964 Forces on a sphere accelerating in a viscous fluid. *J. Fluid Mech.* **18**, 302–314.

Proudman, I. & Pearson, J. R. A. 1957 Expansions at small Reynolds numbers for the flow past a sphere and circular cylinder. *J. Fluid Mech.* **2**, 237–262.

Saffman, P. G. 1965 The lift on a small sphere in a slow shear flow. *J. Fluid Mech.* **22**, 385–400.

Saffman, P. G. 1968 Corrigendum. *J. Fluid Mech.* **31**, 624.

Sano, T. 1981 Unsteady flow past a sphere at low Reynolds number. *J. Fluid Mech.* **112**, 433–441.

Yang, S. & Leal, L. G. 1991 A note on memory integral contributions to the force on an accelerating spherical drop at low Reynolds number. *Phys. Fluids* A **3**, 1822–1824.